Journal of Manufacturing Processes 156 (2025) 509–524

Contents lists available at ScienceDirect

Journal of Manufacturing Processes

journal homepage: www.elsevier.com/locate/manpro

Acoustically assisted additive manufacturing by laser powder-bed fusion of AlSi10Mg

O. Maurer [a,b,*], D. Bähre [a,b]

[a] Institute of Production Engineering, Saarland University, 66123, Saarbrücken, Germany
[b] Centre forMechantronics and Automation Technology (ZeMA), 66121, Saarbrücken, Germany

ARTICLE INFO

Keywords:
Additive manufacturing
L-PBF
Acoustic assistance
Hybrid manufacturing

ABSTRACT

The exceptional design freedom offered by additive manufacturing, including the ability to create complex geometries and graded materials, along with its immense lightweight construction potential, are often cited as compelling advantages of the technology. However, these benefits are counterbalanced by challenges such as poor surface quality in the as-built state. Additionally, the formation of porosity, which has yet to be fully mitigated through parameter optimization, significantly diminishes cyclic strength, particularly when pores are located near the surface. Porosity also contributes to the high variability in physical properties, necessitating its reduction or complete elimination to ensure high reliability, consistent process performance, and long-term durability of the manufactured components.

To address these issues, tailored sonication during the build process could offer multiple benefits for both the powder-bed and the emerging component. Initial prototypes and proofs of concept have been developed for Laser Metal Deposition (LMD) systems. However, the integration of an acoustic transducer into a Laser Powder-Bed Fusion (L-PBF) machine remains a challenge, posing numerous interdisciplinary questions in areas such as physical acoustics, mechanical engineering, materials science, and manufacturing technology. This study seeks to develop a functional acoustically assisted additive manufacturing system based on L-PBF. It focuses on designing an effective transducer, understanding the behavior of powder under acoustic excitation, and evaluating the resulting key properties of the manufactured parts.

1. Introduction and state of the art

Additive Manufacturing (AM) of metals has generated significant enthusiasm within the scientific community. The ability to design components with exceptional geometrical freedom allows for the production of highly complex, lightweight, and customized parts, expanding the range of manufacturable designs [1]. However, despite this flexibility and the excitement surrounding AM, several limitations and challenges hinder the widespread industrial adoption of metal AM technologies. Firstly, build jobs in AM are time-intensive, often requiring hours to complete [2] and part quality decreases as build rates increase. Second, AM-processes produce rough surfaces in a range of $16\,\mu m \leq R_z \leq 175\,\mu m$ depending on the material [3,4]. These rough surfaces significantly reduce fatigue life unless post-processing is applied to smooth them [5]. When all geometrical freedom is exhausted in AM, post processing tools do not have access to internal surfaces of complex shapes [2]. Thirdly, porosity is a critical issue in AM, leading to weakness under both quasistatic and fatigue loads [6,7]. These flaws can even increase their large impact when they form close to a surface [7]. Especially for complex, thin-walled structures, all defects in the material can be considered as close to the surface and clearly force failure mechanisms [7]. While parameter optimization has been able to minimize porosity, complete elimination remains unattainable [8]. To address all of these challenges, this study explores the integration of a hybrid manufacturing concept into Laser Powder-Bed Fusion (L-PBF).

Due to various physical and equipment-related hurdles, publications on acoustic assistance of AM-processes rather deal with Laser Metal Deposition (LMD). Most studies on acoustic assistance in AM focus on Laser Metal Deposition (LMD), largely due to physical and equipment-related complexities. Research in LMD has demonstrated promising results, with studies documenting the relationship between relative density, applied acoustic power, and frequency for metallic alloys and

* Corresponding author at: Institute of Production Engineering, Saarland University, 66123, Saarbrücken, Germany.
E-mail address: oliver.maurer@uni-saarland.de (O. Maurer).

https://doi.org/10.1016/j.jmapro.2025.10.098
Received 10 June 2025; Received in revised form 26 September 2025; Accepted 29 October 2025
Available online 10 November 2025
1526-6125/© 2025 The Authors. Published by Elsevier Ltd on behalf of The Society of Manufacturing Engineers. This is an open access article under the CC BY license (http://creativecommons.org/licenses/by/4.0/).

particle-reinforced composites [9,10]. For instance, acoustic assistance has been shown to improve relative density by approximately one percentage point, resulting in a notable increase in strength [6].

Moreover, continuous sonication in LMD affects the solidification of newly applied layers. Normally, laser-based AM produces a columnar crystal growth structure, directed from the laser incidence point toward the substrate, within the characteristic fish-scale-like cells of the microstructure [11]. Todaro et al. [12] attribute a grain refining effect to the phenomenon of cavitation, which creates high densification pressures as cavities collapse. This results in a significantly finer, much more isotropic and equiaxed microstructure [12,13].

Literature on acoustic assistance in LMD thus confirms that sound can achieve significant effects in additively manufactured workpieces. However, the transfer of the technique to L-PBF is still pending. This also implies that the effect of sound in a powder-bed process may differ significantly from those already documented for LMD. One of the most significant differences between LMD and L-PBF is the existence of a powder-bed in L-PBF, so the response of the powder-bed to sound can have a significant impact on the process flow with sonication. Particle damping due to friction and collisions between powder particles apparently contributes to the compaction [14] of a powder-bed by the Hausner ratio [15], but at the same time significantly reduces the flowability of the powder. The Hausner ratio is defined as the quotient of tap and apparent density or the quotient of apparent and tap volume [16]. Limited research has addressed acoustic assistance in L-PBF. Yan et al. [17] applied ultrasound (40 kHz frequency and 60 W power) only during the laser irradiation phase, achieving grain refinement and slight improvements in mechanical properties (e.g., microhardness, tensile strength, and elongation at failure) in samples made from a cobalt-based superalloy. However, the study did not examine the effects on porosity or surface roughness. Guo et al. [18] used audible sound (2000 Hz frequency and 10 μm amplitude) to sonicate the powder-bed during the L-PBF process of 316 L stainless steel from above through the build chamber instead of sonicating from below through the substrate. This publication does not contain any information whether there is a continuous sonication during the entire build job or a selective sonication as in the study of Yan et al. [17]. Still, Guo et al. [18] report a decrease in porosity, a grain refining effect and an increase in the ultimate tensile strength as well as the elongation at failure. Another study [19] using audible sound (white noise at 3.5 W) reported superior compressive behavior in quasistatic experiments if compared to standard L-PBF and resulted in much less scatter in fatigue life in load increase tests.

Overall, literature shows several advantages of acoustic assistance during build jobs in AM processes. Acoustic assistance in L-PBF seems to share these advantages. The current state of research lacks considerations of directly coupled and continuous sonication during build jobs to create effects of continuous powder-bed compaction and to affect solidification during the laser irradiation phase. Challenges arise to adjust powder properties, acoustic transducers and the L-PBF machine to each other in a way that an assisted L-PBF process produces parts of higher quality than a common L-PBF process without compromising machine integrity. This study addresses these challenges by exploring three key areas: the behavior of powder under acoustic excitation, the design of an acoustic extension kit for L-PBF, and the resulting part properties. Particular focus is placed on identifying suitable sonication modes to achieve superior part quality.

2. Materials and methods

2.1. Powder material and its characterization

AlSi10Mg by Nikon SLM Solutions AG (Lübeck, Germany), a common alloy in L-PBF with a high lightweight potential serves as feed stock material. Due to its high thermal conductivity the alloy tends to form minimal residual stresses in comparison to other common L-PBF materials [20,21], which makes it an easy-to-AM material. Table 1 summarizes the chemical composition of the AlSi10Mg-powder used in this study.

Table 1
Chemical composition of the AlSi10Mg-powder used in this study.

Element	Al	Si	Fe	Mg	Mn	Ti	Zn	Others each
Wt%	Bal.	9–11	0,55	0,45	0,45	0,15	0,10	0,05

Beyond its composition, several powder characteristics have a significant influence on its processibility.

2.1.1. Particle size distribution

A laser granulometer HELOS H2482 (Sympatec GmbH, Clausthal-Zellerfeld, Germany) with its software WINDOX 5 analyzed the distribution of particle diameters. Despite cumulative frequency plots versus particle diameter, characteristic diameters d_{10}, d_{50} and d_{90} are calculated. This data serves as the foundation for estimating the displacements that the transducer is expected to induce during an assisted build job.

2.1.2. Morphology

An automated measurement using a digital microscope (VHX7000, Keyence Corp., Osaka, Japan) was conducted to determine the maximum and minimum diameters of 3871 powder particles, enabling the calculation of their aspect ratios by dividing the minimum diameter by the maximum diameter. The closer the aspect ratio is to 1, the more spherical the particle shape.

2.1.3. Powder flowability

Powder flowability was assessed in accordance with EN ISO 4490 [22]. This method does not precisely represent the in-process spreading behavior but provides a standardized evaluation [23]. As prescribed by the standard, Hall funnel is filled with 50 g of powder. The average flow rate, $\frac{dm}{dt}$, is determined by the time required for the powder to flow out through a small cylindrical borehole. Since powder moisture significantly affects flowability, it was measured using a HYTE-LOG 4800 Bd dew-point sensor (Hygrosens Instruments GmbH, Löffingen, Germany).

2.1.4. Apparent density

According to EN ISO 3923 [24], a cylindrical container with a volume of $(25 \pm 0.03)\ \mathrm{mm}^3$, placed beneath a Hall funnel collects powder particles until it is completely filled. A blade removes a naturally formed material cone, ensuring the container is filled precisely to its defined contours. The apparent density is calculated as the quotient of powder mass (full container mass minus empty container mass) weighed on a precision balance AT200 (Mettler Toledo Inc., Columbus, OH, USA) and the container's volume. Three repetitions ensure reliable measurement results.

2.1.5. Powder compaction behavior

The Hausner ratio H typically represents the quotient of tap density in accordance to ISO3953 [25] and apparent density as described previously. However, powder compaction caused by acoustic waves follows other kinematic principles than those of the standard procedure. Consequently, other methods need to quantify this type of powder behavior. To adopt the Hausner ratio for this purpose, an ultrasonic bath EMMI20 (EMAG AG, Mörfelden-Walldorf, Germany) induces the compacted state in a bulk powder that initially exists apparently dense within a cylindrical container, as per EN ISO 3923. The nominal acoustic frequency and power are 45 kHz and 250 W, respectively. Power scales of 50 %, 75 % and 100 % allow estimations of its impact on compaction. Beyond these nominal values, a wide band of audible frequencies appear and excite the powder sample, so instead of a single frequency a rather noisy excitation causes compaction. Sound waves from the ultrasonic

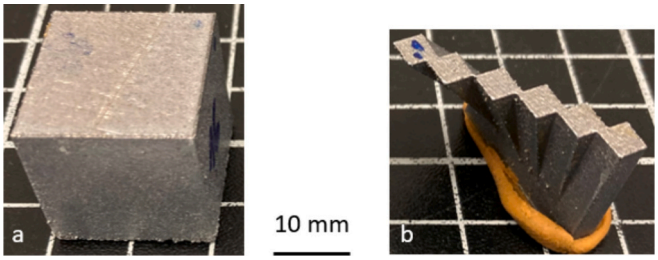

Fig. 1. Sample geometries to qualify assisted L-PBF a) cube sample for roughness and density measurements as well as metallographic preparation and b) fan-sample for roughness measurements depending on the inclination angle.

transducer travel through a steel tub, a water bath, and an aluminum container before reaching the powder sample. Along this path, acoustic insulation occurs due to differences in acoustic impedance. With the acoustic impedances of steel (46.4 MRayl [25]) and water (1.56 MRayl [25]), the transmission coefficient is approximately 0.13, reducing the maximum acoustic power reaching the aluminum container from 250 W to approximately 31 W. As a result, the observed powder compaction behavior is influenced by a broad frequency spectrum at power levels of $\leq$31 W. Three-dimensional imaging using the aforementioned digital microscope provides visualizations of compaction zones and enables the determination of curvature radii on the powder surfaces.

2.1.6. Particle damping

During sonication, the powder is expected to compact according to the acoustic Hausner ratio. A powder-bed has to dissipate acoustic energy to achieve the capability to increase its density. Measurements of particle damping address regimes of high dissipation with respect to exciting acceleration and frequency. A TV51120-C shaker (Tira GmbH, Schalkau, Germany) with a maximum excitation of 200 N in force or 51 *g* in acceleration covers a frequency range from 10 Hz to 25,000 Hz. During testing, either force or acceleration is controlled while the other parameter is measured. The phase angle between the periodic force and acceleration signals indicates the degree of energy dissipation. Throughout the experiments, a force-controlled setup was found to provide clearer and more reliable results.

2.2. L-PBF machine

An SLM125 machine (Nikon SLM Solutions AG, Lübeck, Germany) served as a platform to establish a first acoustically assisted L-PBF setup. All adjustments presented in this study apply to this machine and it fabricated all samples to demonstrate the potential benefits of acoustic assistance during build jobs.

The machine features a cubic build volume of 125 mm edge length and the capability for a build volume downsizing (BVD) to a smaller cube with an edge length of 50 mm. In the standard configuration, the substrate is heated to 423 K (150 °C) for AlSi10Mg to minimize thermal stress formation during the build job. However, downsizing the build volume prevents substrate heating due to the need for a piston to be mounted where the heated substrate would typically reside.

In this study, the build volume downsizing was adjusted due to the possibility to re-design its piston and, by that, to implement an acoustic transducer there. To evaluate the effects, a three-way comparison was conducted: standard L-PBF samples were compared to L-PBF samples fabricated without substrate heating and acoustically assisted L-PBF samples. This approach aimed to determine whether the assisted L-PBF process merely compensates for the absence of substrate heating or genuinely improves part quality.

Table 2
L-PBF parameters for sample fabrication as characterized in [26,27].

Parameter	Powder layer thickness	Laser power	Scan speed	Hatch distance	Scan strategy	Shielding gas
Value	30 µm	250 W	1650 $\frac{mm}{s}$	0.13 mm	Hatch	Argon

2.3. Sample characterization

2.3.1. Sample geometries and fabrication

Two different types of samples are fabricated to assess manufacturability. These parts are used to characterize relative density, surface quality, and microstructural features. Fig. 1 illustrates all geometries and specifies the measurements they are designed for.

The L-PBF parameter set characterized in [26] applies here for sonication in assisted build jobs. Table 2 summarizes key parameters. This set remained consistent across different sonication modes.

Despite manually sawing samples off their substrate and support removal, samples remained in the as-built state. No post-processing techniques apply to assess the untouched fabrication result.

2.3.2. Archimedean density measurements

Relative density marks a counterpart to porosity. The precision balance AT200 as mentioned before equipped with an Archimedean density setup weighs samples three times in ambient air and three times in water immersion. The temperature of the water bath is measured to read its density off a table. Using the theoretical mass density of the alloy, $\rho_{th} = 2.67\ g/cm^3$ [28], the sample masses in air m_a and in water m_w along with the density of the water bath $\rho_w(T)$, the relative density is defined as:

$$\rho_r = \frac{1}{\rho_{th}} \frac{m_a\, \rho_w(T)}{m_a - m_w} \tag{1}$$

Measurement errors were calculated based on the gaussian law of error propagation as given in Eq. 2.

$$\Delta\rho_r = \frac{\rho_w(T)}{\rho_{th}\,(m_a - m_w)^2} \sqrt{m_a^2 \Delta m_a^2 + m_w^2 \Delta m_w^2} \tag{2}$$

Δm_a and Δm_w represent standard deviations of samples masses weighed in both media.

2.3.3. Computed tomography (CT)

Cubes with an edge length of 8 mm were cut from cube samples of Fig. 1 a) to obtain 10 µm resolution in the setup CT-alpha (Procon X-ray GmbH, Sarstedt, Germany) at Fraunhofer IZfP (Saarbrücken, Germany). Measured data underwent a reconstruction and 3D segmentation in 3D-slicer freeware [29].

2.3.4. Metallographic preparation

To assess the porosity level indicated by relative density values, samples are ground on SiC sandpaper (320–2500 graining) and polished with textile cloths (6 µm and 3 µm diamond suspension, followed by OPS suspension) before pore analysis with the digital microscope.

2.3.5. Surface quality assessment

According to EN ISO 13565 [30], the central core roughness R_k and peak core roughness R_{pk} characterize each as-built surface after measurement with stylus profilometry of a Perthometer PGK120 (Mahr GmbH, Göttingen, Germany). The division into central and peak regions allows differentation between central roughness induced by layered structure on a side plane or laser scan paths on an upskin plane, and peak roughness from mainly particle adhesion. These values are derived from a cumulative frequency plot of an original roughness profile, known as the Abbott-Firestone curve. The original roughness profile consists of

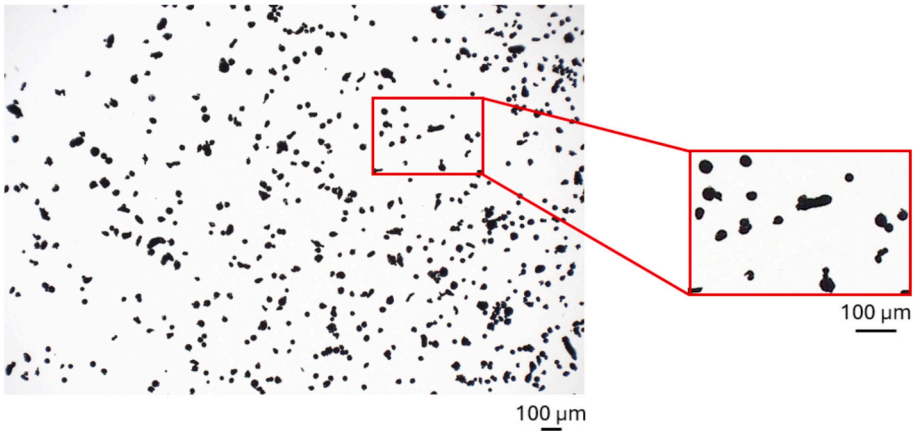

Fig. 2. Optical micrograph of the AlSi10Mg powder used in this study.

Table 3
Standard powder properties of AlSi10Mg powder used in this study.

Powder property	Virgin powder	State
Relative moisture content /%	8.87	Not sieved
Flowability /**g**/**s** (EN ISO 4490)	0.61 ± 0.01	
Apparent density /**g**/**cm**^{3} (EN ISO 3923)	1.29 ± 0.01	
Maximum diameter of 10 % of particles $\boldsymbol{d_{10}}$ /µm	26.28	
Maximum diameter of 50 % of particles $\boldsymbol{d_{50}}$ /µm	43.29	
Maximum diameter of 90 % of particles $\boldsymbol{d_{90}}$ /µm	68.59	

five scan lengths of 2.5 mm each, along with two 1.25 mm scan lengths at the beginning and end of each track for transient oscillations, resulting in a total contact length of 15 mm. Additionally, a waviness filter of 2.5 mm in wavelength applies.

2.3.6. *Microstructural analysis*

After metallographic sample preparation, electron backscatter diffraction (EBSD) measurements reveal grain shapes and orientations in the inspected area. Measurements were performed using a scanning electron microscope (SEM) Sigma VP (Carl Zeiss AG, Oberkochen, Germany) equipped with an EBSD detector Nordlys (Oxford Instruments PLC, Abingdon, UK) in a scanned area of 200 µm by 200 µm and a step size of 1 µm. The data obtained from the EBSD analysis were evaluated using EDAX OIM software (Ametek Inc., Berwyn, PA, USA) and ATEX freeware [31] to analyze microstructural features and texture.

3. Powder behavior

3.1. *General powder characterization*

Several powder properties like moisture, flowability, apparent density and particle size distribution belong to a standard set of quality assuring tests. Fig. 2 displays an optical microscopy image (recorded using a VHX 7000 by Keyence Corp., Osaka, Japan) of the powder used in this study. Further powder characterization such as chemical composition analysis was presented in a previous study [27]. Flowability gives a first insight into in-process spreading behavior. Since this is a common L-PBF powder, spreading works sufficiently if the relative moisture content does not exceed 10 %.

Apparent density measured according to standard EN ISO 3923 as given in Table 3 lies in a similar range like values from literature 1.46 $\frac{g}{cm^3}$ [32] and 1.43 ± 0.07 $\frac{g}{cm^3}$ [33]. Differences may result from different particle size distributions and different moisture contents leading to different cohesion behavior of bulk powders.

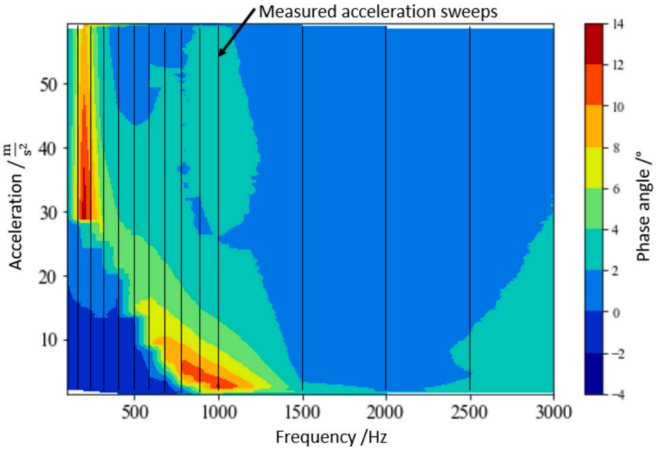

Fig. 3. Energy dissipation heat map based on acceleration sweeps at discrete frequencies (black marks) and linear interpolation inbetween; the discrete frequencies chosen for acceleration sweeps are: from 100 Hz to 1000 Hz in steps of 100 Hz, 1500 Hz to 3000 Hz in steps of 500 Hz.

3.2. *Particle damping*

A rather unconventional characterization technique, particle damping, assesses acoustic or vibration-related powder properties. For compaction, a powder-bed has to absorb vibrational energy manifesting itself in a large amount of dissipation. Acceleration sweeps at discrete frequencies lead to dissipation heat maps as a function of the phase angle, see Fig. 3.

Obviously, two regions reach high dissipation, frequencies around 200 Hz at 30 $\frac{m}{s^2} - 35 \frac{m}{s^2}$ and frequencies around 1000 Hz at 1 $\frac{m}{s^2} - 5 \frac{m}{s^2}$. It depends on the excitation and the powder-bed volume, which frequency matches the pursued assisted L-PBF process best. The volumetric dependency decreases in favor of build direction dependency due to the constant powder-bed base area and the use of a transducer oscillating along the build direction. Both hotspots imply strong dissipation of vibration energy of a bulk powder. Dissipation does not necessarily mean powder compaction. After the particle damping experiments, closed particle containers do not allow for measuring powder flowability, but they are made from transparent polymers and the behavior of the bulk powder if the container is turned upside down can be observed. In the case of 200 Hz, powder seems to behave in the same way as before excitation. With 1000 Hz the bulk powder reaches a higher level of cohesion with reduced flowability, which proves compaction. This implies that samples with a sonication at 200 Hz cannot profit from a compacted powder-bed, whereas samples with a sonication of 1000 Hz

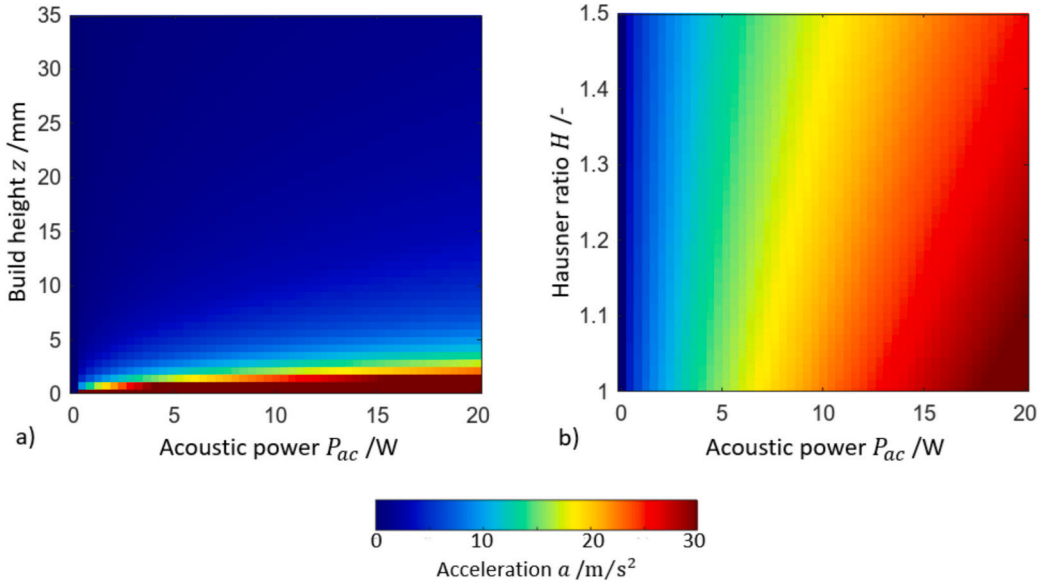

Fig. 4. Distribution of acoustic acceleration as calculated in Eq. 5 depending on a) build height and acoustic power at H = 1 and b) Hausner ratio and acoustic power at z = 35 mm.

can.

Estimations of the acceleration distribution base on the assumption that a powder-bed was a continuous bulk body. Its acoustic impedance Z_{PB} is determined using a mixing rule that depends on acoustic impedances of aluminum and argon, Z_{Al} and Z_{Ar}, as well as the apparent density ρ_A, the theoretical density of the alloy ρ_{th} and the powder's Hausner ratio H.

$$Z_{PB}(H) = \frac{\rho_{th} - H\,\rho_A}{\rho_{th}} Z_{Ar} + \frac{H\,\rho_A}{\rho_{th}} Z_{Al} \tag{3}$$

A force equilibrium m a = F = p A including the excited mass m and effective acoustic pressure p leads to an equation that describes the acceleration inside a powder-bed. In consideration of changes in powder masses as a consequence of layer application, the mass as a function of build height z is defined as:

$$m(H, z) = H\,\rho_A\,A\,z \tag{4}$$

With the effective acoustic pressure depending on the acoustic power supply P_{ac}, it is $p = \sqrt{\frac{Z_{PB}\,P_{ac}}{A}}$ derived from [34]. The acoustic acceleration is then calculated considering an overall transmission coefficient from the transducer to the powder bed of t = 0.0079:

$$a(H, z, P_{ac}) = \sqrt{\frac{Z_{PB}(H)\,t\,P_{ac}}{A}}\,\frac{1}{\rho_A\,z} \tag{5}$$

Color maps as depicted in Fig. 4 display the function above depending on two out of three key parameters, which represent powder compaction, build height and acoustic power input.

Fig. 4 a) proves that accelerations significant for AlSi10Mg powder compaction at 200 Hz only are confined to a build height of only a few millimeters within an acoustic power range of up to 20 W. In the very same power range, accelerations of a build height up to 35 mm match the dissipation regime for compaction of 1000 Hz as depicted in Fig. 3. This explains, why samples of particle damping showed different degrees of flowability after excitation with 200 Hz and 1000 Hz at the corresponding acceleration for high energy dissipation. At 200 Hz, only a small layer of a few millimeters compacts while the rest remains close to the apparent density and flowability. At 1000 Hz, the whole powder sample compacted and lost flowability. As shown in Fig. 4 b), an increasing Hausner ratio results in a decrease in the acoustic impedance of the powder-bed, reducing its resistance to sound propagation and leading to higher accelerations at a fixed z. The acoustic power range considered aligns with commercially available transducers that emit audible sound.

3.3. Compaction behavior

Quantitative experiments on the AlSi10Mg powder compaction behavior shall clarify possible effects and applicability of large compactions to the L-PBF process. First experiments take place in an

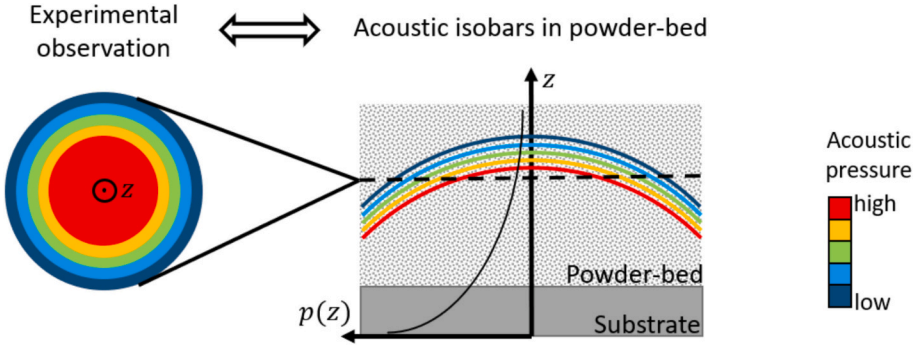

Fig. 5. Schematic sketch that explains formation of differently compacted zones.

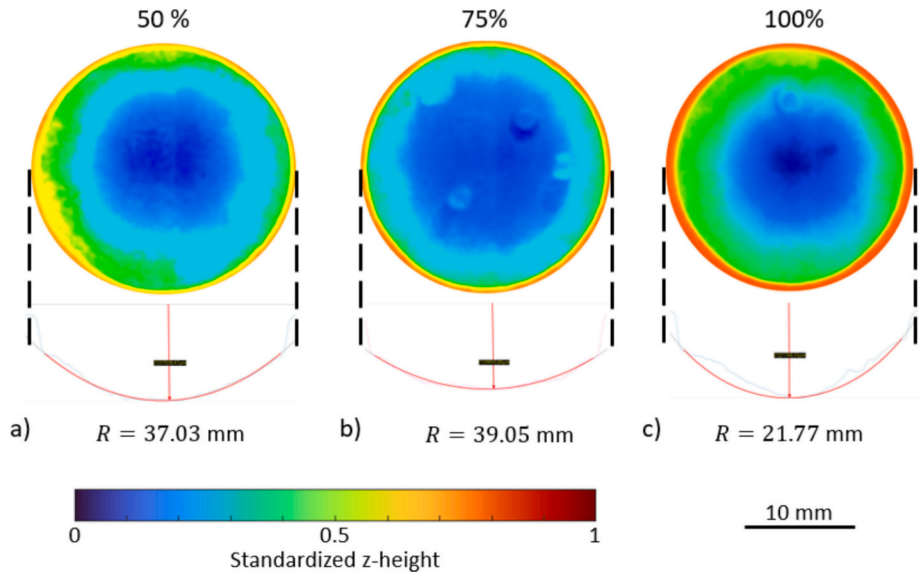

Fig. 6. Experimentally verified compaction zones and radii of curvature along the diameter after sonication in the ultrasonic bath at power levels a) 50 %, b) 75 % and c) 100 % and an entirely filled container.

Table 4
Results of powder compaction experiments in an ultrasonic bath.

Power level /%	Powder mass /g	Apparent density /g/cm3	Hausner ratio edge /–	Hausner ratio center /–
100	33.587	1.34	1.26	1.52
75	33.450	1.34	1.14	1.26
50	34.487	1.38	1.10	1.22

ultrasonic bath Emmi20 (EMAG AG, Mörfelden-Walldorf, Germany). The aluminum container used for apparent density measurements is placed in the middle of the ultrasonic bath, which is filled with water. A potentiometer allows to choose acoustic power levels of 50 %, 75 % and 100 % of maximum 250 W at a nominal frequency of 45 kHz. During operation, the device emits audible sound in a wide frequency band, so the excitation uses more than one sharp ultrasonic frequency. Power transmission losses decrease the real acoustic power which leads to compaction. The transmission coefficient from steel tub to water bath amounts 0.12 which means a maximum acoustic power of 30 W inside the bulk powder in this experiment.

Powder in a state of apparent density compacts within a timespan of approximately 10 s while forming a concavely shaped spherical surface displaying the inverted curvature of sound wave fronts. Color codes in Fig. 5 rank acoustic pressure levels from low to high in a qualitative manner with respect to sound attenuation in growing distances to its source. Consequently, concentric compaction zones emerge in a sectional view and recommend a round substrate for more homogeneous sound propagation across the powder-bed surface.

Experimental powder-bed surfaces display this effect regardless of the exciting acoustic power. As depicted in Fig. 6, powder heights inside the container (color codes blue, green or yellow) differ from the container's edge height (color codes orange or red) forming a curved profile. Artifacts on powder-bed surfaces occur due to water droplets entering the container during sonication in the ultrasonic bath, but a few drops do not significantly affect measurement results.

Changes in height of bulk powders, measured before and after sonication, as well as differences observed at the edges and center of the microscopy images, enable the calculation of Hausner ratios, as shown in Table 4. Apparent density calculations shall validate Hausner ratios. They are similar to the standard-conforming data from Table 3. Hausner ratios do not exceed their theoretical maximum value $H_{max,th}$ deriving from a densest packing of spheres of 0.74 [35]. So 74 % of the theoretical density $\rho_{th} = 2.67\ \frac{g}{cm^3}$ [28] mark the densest state of a bulk powder and if divided by the apparent density ρ_A it is:

$$H_{max,th} = \frac{0.74\ \rho_{th}}{\rho_A} \approx 1.53 \tag{6}$$

Different degrees of compaction described by an interval of Hausner ratios cover surface curvatures of sonicated bulk powders. Such curvatures on the top of a powder-bed in a L-PBF process would probably lead to failed build jobs due to inhomogeneous layer thicknesses. However, these experiments neglect the layer-by-layer fashion and focus on compaction of a large powder volume allowing for cascading compaction through the entire volume. In an assisted L-PBF process, thin layers <100 µm would spread on an already compacted powder-bed. Furthermore, the recoater spreads a flat layer and removes forming curvatures of the powder-bed. In conclusion, curvature shows compaction zones and proves Fig. 5 to explain observations validly, but do not harm build jobs after implementation of the technique.

These results of compaction in an ultrasonic bath and its theoretical background enable calculations of the compaction distribution in a powder-bed as a function of radius r and height z in a cylindrical build volume. Boundary conditions following the pressure drop from p_0 along a growing distance from a transducer are for the density of a powder-bed ρ_{PB} at the substrate ($z = 0$) and in infinite build heights ($z \to \infty$):

$$\rho_{PB}(z = 0) = H\ \rho_A; \rho_{PB}(z \to \infty) = \rho_A \tag{7}$$

This results in a powder-bed density along z given by:

$$\rho_{PB}(z) = \frac{(H - 1)\ \rho_A}{z + 1} + \rho_A \tag{8}$$

Within a powder layer, due to the curved wave fronts, there is a radial dependence of the density $\rho_{PB}(r)$ as the observed compaction zones prove. Rotational symmetry can be assumed in the analytical view so that only the radial position is included in the derived function without the angular information. The height of the powder-bed surface curvature with radius R after compaction, starting from the height z at the center of the recoating plane, is given by:

$$\Delta z(r) = R + \sqrt{R^2 - r^2} \tag{9}$$

The radial distribution for ρ_{PB} is then given by the reduction of the apparent volume divided by the radially distributed volume at different

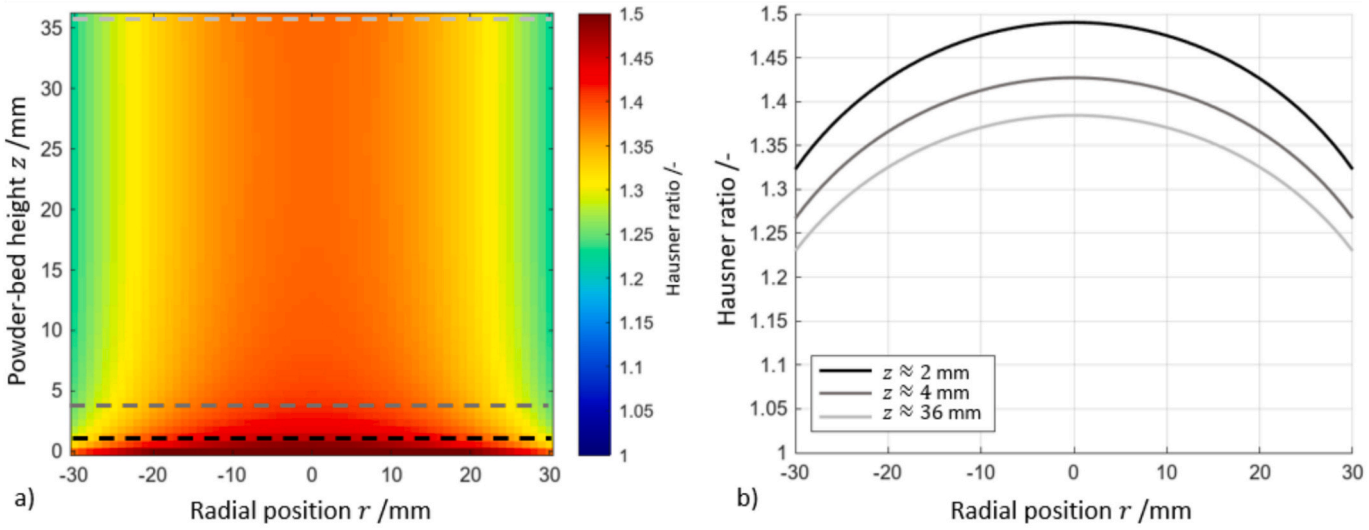

Fig. 7. Compaction distribution in a sonicated powder-bed with dimensions of 60 mm in diameter and 36 mm in height a) heat map of H(r,z) and b) compaction profiles of different build heights z.

z-heights:

$$\rho_{PB}(r) = \frac{z}{\Delta z(r)}\,\rho_A = \frac{z}{R+\sqrt{R^2-r^2}}\,\rho_A = H(r)\,\rho_A \rightarrow H(r) = \frac{z}{R+\sqrt{R^2-r^2}} \tag{10}$$

This notation of $H(r)$ emphasizes the role of cascading compaction by including the height z. It gives relative portions of compactions in %, while $H(z)$ gives absolute Hausner ratios. In multiplicative linking of both information for a compaction chart in cylindrical coordinates $H(r,z)$, it is:

$$H(r,z) = \left(\frac{H(r)}{100}+1\right) H(z) \tag{11}$$

The mean surface curvature of compacted bulk powders amounts 36.95 mm, which leads to the heat map in Fig. 7 a), if the cylindrical build volume has a diameter of 60 mm and a height 36 mm. Compaction profiles of fixed heights are shown in Fig.7 b).

Fig. 7 illustrates quantitatively how compaction zones form during an assisted L-PBF build job. It still depends on the acoustic power which was not explicitly part of model equations. However, possible gradients of part quality features affected by powder-bed compaction become evident after these considerations.

4. Components of an extension kit

4.1. Transducer design

A suitable transducer has to meet several requirements to ensure a successful L-PBF build job which is continuously sonicated. These are:

- Encapsulation to protect its electronic circuits from powder
- Compact style for a preferably large build volume
- Sufficient acoustic power emission including an adjustable acoustic signal
- Thermal stability for resistance against process heat brought in by the laser

Structure-borne sound transducers fulfill the first two of four requirements. The transducer Eliga 85,977 (Elsässer GmbH, Augsburg, Germany) chosen for this study is originally designed to play music in warm environments and reaches a nominal thermal stability up to 358 K (85 °C). Temperature profiles from two Standard-L-PBF build jobs without substrate heating (373.75 K at 20.6 % areal occupancy, 375.35 K at 47.7 % areal occupancy) allowed for a rough linear estimation of maximum temperatures in a substrate T_{max} as a function of the relative areal occupancy of the substrate b in %. It is:

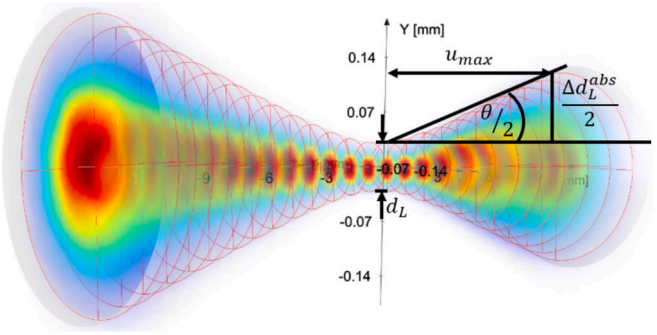

Fig. 8. Dimensioned intensity profile around the focal plane of the laser inside the SLM125 in new condition; u_{max} maximum allowable acoustic displacement, θ angle of beam divergence, d_L focal diameter, Δd_L^{abs} absolute diameter deviation from focus.

$$T_{max} = 0.06\frac{K}{\%}\,b + 372.53\ K \tag{12}$$

According to this formula, a high areal occupancy b = 90% would result in a temperature of approximately 378 K (105 °C). By that, it would exceed the nominal limit. Experiments will test whether this limit stands or not, since there are no other encapsulated transducers on the market with higher thermal stability.

The Eliga 85,977 works within the audible sound range. Particle damping experiments already gave the hint that audible frequencies surpass the performance of ultrasonic frequencies. The main reason is the relationship between acoustic acceleration a, displacement upon vibration u and angular frequency ω, which is $u = \frac{a}{\omega^2}$. So, the higher the frequency the lower is the displacement of this vibration. Hence, it means a decreasing effect on the powder-bed at a constant acoustic power level, which influences the acceleration.

The focal plane of the laser beam is positioned at the current powder-bed surface. A vibration along *z* lifts this surface out of focus, which can lead to deviations in the beam diameter, dimensional accuracy and other component properties depending on the laser spot size. Therefore, increasing the beam diameter puts a maximum limit to the displacement

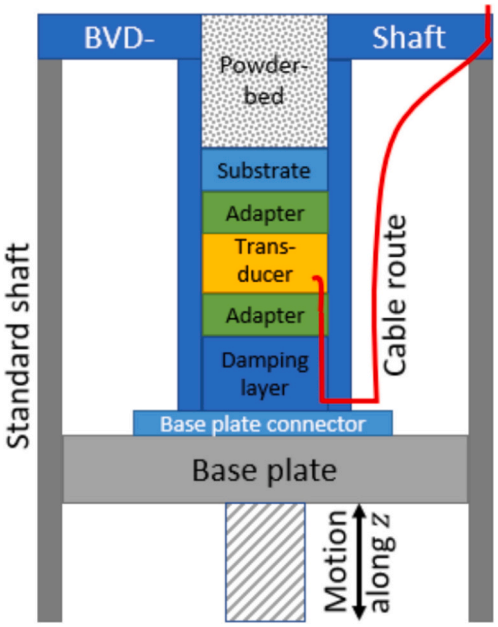

Fig. 9. Schematic sketch of the adjusted build volume downsizing for assisted L-PBF inside the standard shaft.

along z. The laser system of the SLM125 machine was characterized in new condition. The measurement protocol from Cinogy Technologies GmbH shows relevant values for the laser divergence. Fig. 8 shows the measured shape of the laser beam including the intensity profiles of each plane and the geometric variables.

From geometry derives:

$$\tan\left(\frac{\theta}{2}\right) = \Delta\mathrm{dLabs2u_{max}} \tag{13}$$

The beam divergence angle in radians is calculated according to [36] from the wavelength of the light $\lambda = 1.07\ \mu$m, the beam quality factor $M^2 = 1.111$ and the focal diameter $d_L = 61.7\ \mu$m:

$$\theta = M^2 \frac{4\lambda}{\pi d_L} \tag{14}$$

If a maximum relative deviation in beam diameter of $\Delta d_L^{rel} = 2\%$ allowed in the process, and $\Delta d_L^{abs} = \left(1 + \Delta d_L^{rel}\right) d_L$, the maximum displacement is derived from Eqs. 13 and 14:

$$u_{max} = \frac{\left(1 + \Delta d_L^{rel}\right) d_L}{2 \tan\left(M^2 \frac{4\lambda}{\pi d_L}\right)} = 50.3\ \mu\mathrm{m} \tag{15}$$

In conclusion, the transducer should not induce displacements greater than 50 µm to avoid significant beam widening on the powder-bed surface, which could result in lower geometrical accuracy. Only low frequencies within the audible sound range reach this limit. Frequencies of interest, based on particle damping measurements, fall below this threshold (with $u_{max} = 19$ µm at $a = 30\ \frac{m}{s^2}$ and $f = 200$ Hz), but still induce motion in the assisted L-PBF process. Ultrasound could only hold up to this, if much larger accelerations forced by much larger acoustic power apply. So, this proves why audible sound is the more efficient choice.

4.2. Adjustments of build envelope downsizing

All changes in the machine environment are limited to the build chamber of the L-PBF machine, in particular to the build volume downsizing (BVD). This limitation arises because the machine features a base plate on the traversing unit, which has been calibrated by the manufacturer for component mounting. However, sensitive sensors and heating electronics are located beneath the base plate, necessitating this restriction. A reduced shaft encloses the movable piston, whereby a TPU seal, which was additively manufactured with Fused Filament Fabrication (FFF), separates the two parts from each other and ensures powder tightness. The reduced shaft size creates spaces in the intermediate areas between the standard and downsized shaft, which are suitable for routing the transducer cables. Fig. 9 illustrates the components of the piston and a possible cable routing path through the shaft. The damping layer reduces the sound intensity guided to the L-PBF-machine as most portions shall assist the build process. Cork serves as a damping material for its thermal stability [37] exceeding the aforementioned thermal load of L-PBF. Additionally, its acoustic impedance is much lower than that of steel, which other piston components like adapters and base plate connector are made of. This leads to large intensity losses during the transmission of sound from steel to cork and again to steel.

Most parts of the piston are joined with a high temperature silicone glue. Only the substrate is fixed with two screws on its adapter, the base plate connector is fixed with four screws on the base plate and the transducer's capsule has a threaded sleeve (Whitworth W3/16″), which is mounted on a threaded rod on the adapter below. This design makes the whole setup easily removable from the machine and allows for substrate handling in the same way as in Standard-L-PBF.

The shaft consists of two components and is fixed with eight screws in the build chamber. The spaces in the intermediate area between the BVD shaft and the standard shaft, combined with the movement of the base plate that alters this space, create a need for pressure equalization between this area and the build chamber. Therefore, there is a hole in the horizontal part of the shaft, which is covered by glueing in a piece of felt, so gas can pass through and powder cannot.

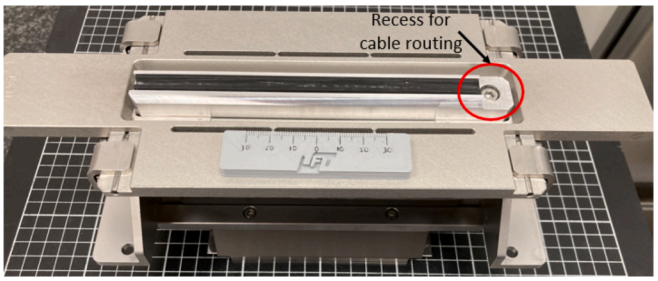

Fig. 10. Bottom of the recoater with the adjusted rubber strip holder to avoid collisions with routed cables, scale in mm.

4.3. Cable routing

The adapter between the transducer and the damping layer ensures powder tightness by using a seal that presses against the shaft wall. Additionally, it has a hole in its center to guide transducer cables through the inside. Recesses in the damping cork and the bottom of the shaft allow for the cable to route toward the build chamber. In the build chamber, cables must lie as flat as possible to avoid interference or collisions with the recoater. For that reason, its holder of the rubber strip, which is responsible for a smooth powder layer distribution, is remodeled with a recess at the side as illustrated in Fig. 10. Afterwards, the recoater does not collide with cables and still spreads a smooth and homogeneous layer in the BVD-setup as well as in the standard setup with a much larger substrate.

After cables passed the recoater, they are routed to an edge of the build chamber and move along the edges until it reaches the pipe end offering an exit out of the build chamber in a gas-tight fashion. Usually, a lid covers the pipe end and assures tightness. Cable glands of type 52,015,710 (Lapp Holding SE, Stuttgart, Germany) inserted into this lid with a PG9 thread shall clamp cables so tight that no gas can pass

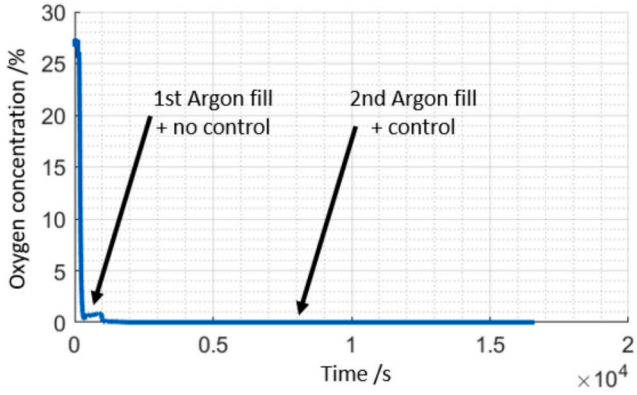

Fig. 11. Result of gas tightness test after cable routing from the inside of the build chamber to the outside.

through.

Gas tightness of the entire build chamber is tested by reducing the oxygen concentration inside to approximately 2 % while filling the chamber with argon. Then, the evolution of the oxygen content, if neither gas circulation nor gas control system is turned on, reveals gas tightness with constant oxygen levels. Afterwards, a complete build job including gas circulation and gas control system proves gas tightness with its argon consumption in comparison to jobs before the adjustments.

Fig. 11 shows a small rise in oxygen concentration after the first argon fill, which probably results from excess oxygen in the pipe system or the gas circulation filter. The second fill and subsequent run of a build job including gas control ensured a stable oxygen level. The consumption of argon in this build matches the usual consumption of build jobs leading to a pressure drop of 10 bar – 15 bar in the argon cylinder. So, the adjusted L-PBF machine is gas tight and can operate without higher argon consumption.

4.4. Control of the acoustically assisted setup

Almost any sonication mode with single frequencies, superposed frequencies or noise of any color can be realized with the freeware Audacity. For this purpose, a control computer, which is not integrated into the L-PBF machine, is available. Via an AUX connection, which is common in public address (PA) technology, the computer sends sound signals to a power amplifier The t.amp E400 (Thomann GmbH, Burgebrach, Germany), which transmits the signal with the appropriate power to the converter via commercial speaker cables. To ensure that the control and monitoring circuitry can withstand continuous operation, the power amplifier must have a significantly higher maximum output than required for operation. The transducer can take up 20 W maximum and has a nominal impedance of 8 Ω. An 8 Ω output of this amplifier delivers up to 120 W, which is six times the maximum transducer power. This ensures that the amplifier can withstand continuous operation.

Acoustic power is measured using two voltage measurements: U_S across a shunt resistor of $R_S = 0.1\ \Omega$ and U_0 across the voltage source. Since $P = U\,I$, and by applying Kirchhoff's loop law and Ohm's law, the relationship can be derived as follows:

$$P = (U_0 - U_S)\,\frac{U_S}{R_S} \tag{16}$$

This power calculation from Eq. 16 is based solely on RMS values of two measurement channels of a digital oscilloscope PicoScope 2204 (Pico Technology Ltd., St. Neots, UK) and the PicoScope 7 T&M software. Voltage probes Voltcraft PP-80 (Conrad Electronic SE, Hirschau, Germany) are connected to the oscilloscope inputs. In addition, this form bypasses the frequency-dependent effective resistance of the transducer, whose nominal impedance divides into real and imaginary parts depending on the frequency. This results in a robust measurement of the acoustic power.

Power output and frequency response in Fig. 12 a) and b) depend on the whole transducer setup and the way the transducer is mounted. The potentiometer of the amplifier has scale divisions from 0 to 21 and transducers fail from scale division 15 on, so 0 to 14 marks an operable range. Power output, as sketched in Fig. 12 a), describes a non-linear function with different courses for different sonication modes. Single frequencies like 200 Hz and 1000 Hz provide almost the same acoustic power. Their superposition is stronger due to two overlapping soundtracks, one for each frequency, playing simultaneously. The acoustic power of white noise falls short of the others. Nonetheless, a wide range of frequencies can have a significant influence on the powder-bed. Frequency response of the transducer is subject to large fluctuations. Sound levels emitted with the frequencies of interest do not reach into regions of mandatory personal protective equipment for machine

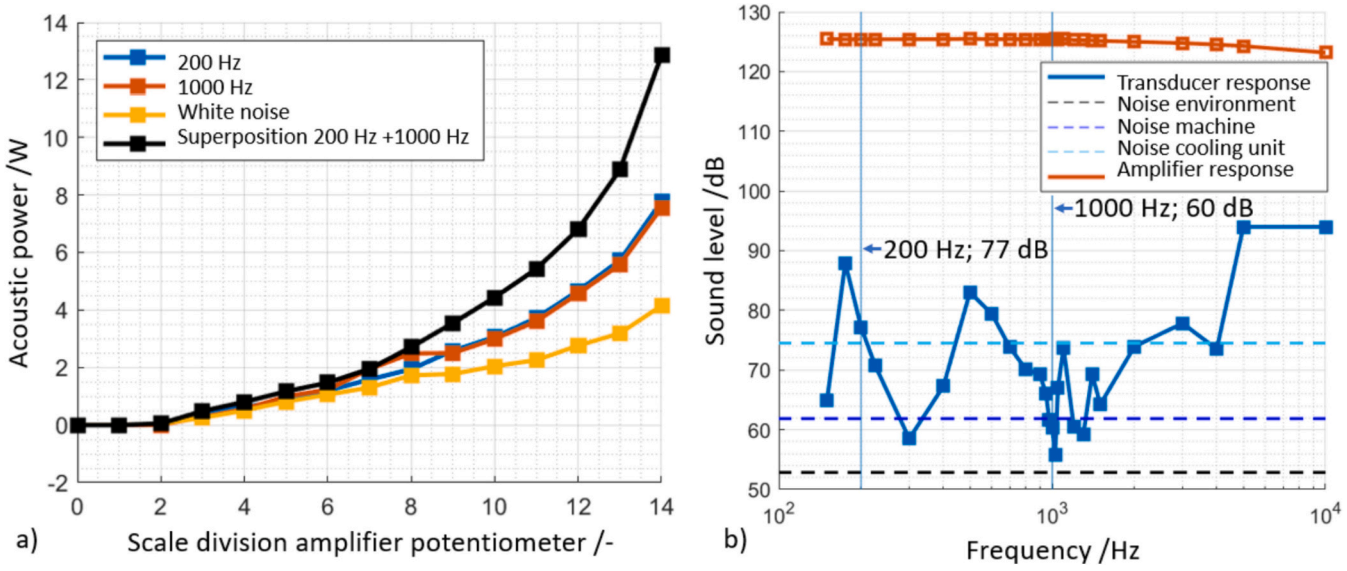

Fig. 12. a) Acoustic power for different sonication modes as a function of potentiometer setting and b) emitted sound level versus frequency on the finished setup with the transducer from Eliga compared to levels from the machine environment or the emitted power level of the amplifier.

Table 5
Results of compaction experiments in the sonication setup used for assisted L-PBF.

Acoustic power /W	Frequency /Hz	Powder mass /g	Apparent density /g/cm3	Hausner ratio edge /–	Hausner ratio center /–
3.1	200	29.949	1.41	1.08	1.09
6.1	200	29.303	1.38	1.14	1.17
3.1	1000	30.347	1.43	1.05	1.08
5.7	1000	29.006	1.36	1.11	1.13
2.1	White noise	29.522	1.39	1.06	1.08
3.5	White noise	29.221	1.37	1.07	1.07

operators as required by German or American health and safety regulations [38,39].

4.5. Compaction assessment in the sonicating setup

In order to verify the observations of compaction experiments in the ultrasonic bath, the aforementioned setup for sonication during L-PBF build jobs was equipped with a polymer container which was screwed onto the adapter on the transducer (nomenclature from Fig. 9). This container had a diameter and height of 30 mm to compact a bulk powder. The analysis was performed as described for the previous compaction experiments. Table 5 gives the results of these experiments. Again, the apparent density values, which are determined by dividing the powder mass by the container volume is in a adequate range. The calculated Hausner ratios do not differ as much as with sonication in the ultrasonic bath, so curvature radii form larger. Especially white noise leads to uniform compaction due to very similar or even identical Hausner ratios in the center and on the edge of the container. Obviously, these compaction values undercut these from the ultrasonic bath. The cause are either the much lower power levels for stable operation or the absence of ultrasonic frequencies. However, plausible compaction can be achieved in a targeted manner and build jobs have to reveal the effects of the corresponding compaction.

5. Resulting part properties

Four different sonication modes shall clarify possible part quality enhancements. Therefore, one build job with the assisted L-PBF setup is conducted for each sonication mode. Build jobs with white noise as well as 200 Hz and 1000 Hz single frequencies succeed, whereas the superposition of 200 Hz and 1000 Hz fails several times due to insufficient bonding of support structures and parts to the substrate. This issue may originate from large displacement amplitudes of two additively superposed frequencies. These defects occur from the first layer on. Using Eq. 5 and $u = \frac{a}{\omega^2}$, the acoustic displacement u can be calculated from acoustic power. So, under the assumption that an initial powder layer is 50 µm thick and using the measured acoustic power levels of scale division 12 from Fig. 12, 200 Hz causes 17.3 µm and 1000 Hz cause 0.7 µm of displacement. A superposition of both frequencies would have a 200 Hz carrier wave resulting in 20.8 µm of displacement. Consequently, the previously calculated displacement threshold has to be corrected to 20.8 µm and only three sonication modes in L-PBF lead to successfully built part geometries as shown in Fig. 1.

Usually, the substrate of the original L-PBF machine SLM125 is heated to 423 K (150 °C) for AlSi10Mg to reduce the formation of thermal residual stresses. Due to the layered setup of the adjusted piston including a damping cork and a transducer with limited thermal stability, there is no possibility to include substrate heating into this prototype. In the following experiments, parts of standard L-PBF including substrate heating (MSH) and standard L-PBF excluding substrate heating (OSH) serve as references to sonicated parts and allow for the assessment of true quality enhancement.

Table 6
Archimedean density of parts fabricated by different L-PBF modes.

Mode	MSH	OSH	200 Hz	1000 Hz	White noise
Acoustic power /W	–	–	7.35	4.82	3.67
Relative density /%	99.70	99.83	99.83	100	100
Error of relative density /%	0.02	0.04	0.04	0.01	0.03

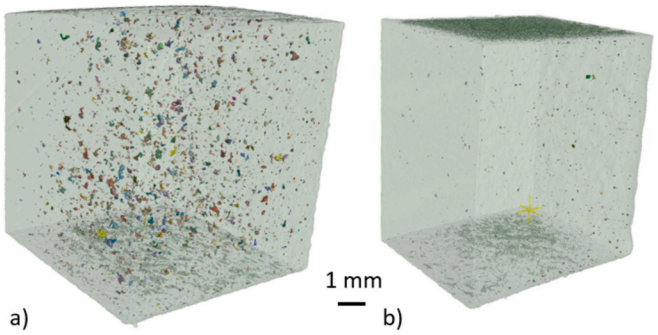

Fig. 13. Illustrative CT-scans of cubes a) standard L-PBF including substrate heating (MSH) and b) assisted L-PBF with white noise.

5.1. Porosity

Powder-bed compaction and sonication of the liquid phase shall reduce porosity. As indicated by Table 6, two out of three sonication modes lead to a relative density of 100 %, which indicates non-porous parts after Archimedean density tests. However, standard deviations imply that the samples are not perfectly dense, which means that a small amount of residual porosity may remain. The relative density after a standard L-PBF build job without substrate heating corresponds to that after a build job assisted with 200 Hz. This confirms the assumption that powder-bed compaction only happens in the support structures due to matching acoustic accelerations, see Fig. 4 a), and that the part remains unaffected due to smaller acoustic accelerations.

Qualitatively, an exemplary CT-scan on sample pieces with an edge length of 8 mm proves a strong decrease in porosity when sonicated with white noise compared to standard L-PBF in MSH mode. These samples are part of cube-shaped samples as depicted in Fig. 1 a), but to reach resolutions that make pores visible 8 mm is the maximum edge length for AlSi10Mg. The number of pores observed in MSH mode, shown in Fig. 13 a), is 2 to 3 times higher than that observed with white noise, as seen Fig. 13 b). Obviously, the segmentations still contain artifacts on sample surfaces due to the software analysis, so the number of detected pores deviates from the real state. These CT-scans prove the existence of residual porosity as indicated by the measurement errors in Archimedean density measurements. Nevertheless, the sample volumes show significant reductions in porosity. This reduction of porosity may be a result of smoother surfaces. Outer surfaces of parts show reduced roughness indices (see subsection 5.2), which also applies to interfaces between powder layers, because they happen to be outer surfaces during the run of a build job. Rough powder layer interfaces lead to porosity [40] and the smoothing effect of acoustic assistance inhibits this mechanism. However, there are several other pore formation mechanisms in L-PBF in general as well as in L-PBF of aluminum alloys particularly. According to Weingarten et al. [41] moist powder leads to the formation of numerous small (about 10 µm) and spherically shaped pores as a consequence of a hydrogen-based effect. Obviously, the CT-scan of Fig. 13 b) reveals small and spherically shaped pores, which proves that sonication cannot eliminate the hydrogen-based pore

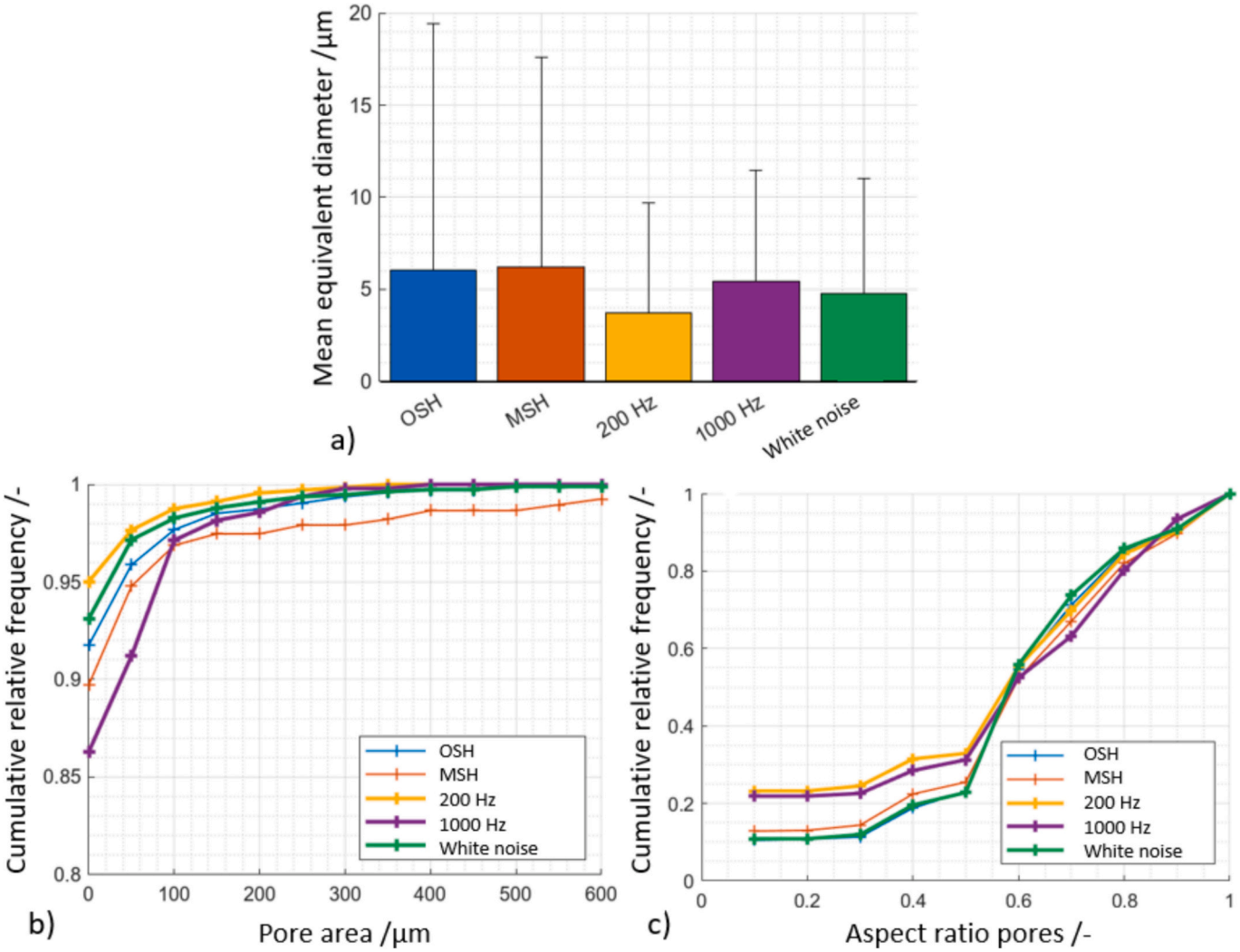

Fig. 14. Statistical pore analysis of metallographic cross sections a) mean equivalent diameter, b) pore area distribution and c) aspect ratio distribution.

formation in aluminum alloys.

Metallographic cross sections serve as a basis for quantitative analysis of pore shapes and sizes. Automated measurements on the digital microscope allow for a statistical evaluation of the pore size distribution. Here, the variables shown in Fig. 14, the mean equivalent pore diameter (a)), the pore area (b)) and the aspect ratio as the quotient of the minimum to maximum diameter of each pore (c)) are used. The mean equivalent pore diameter d_{eq} describes the diameter that an exactly spherical pore with an identical area would have, whereby the average area of all measured pores $\overline{A}$ in a cross section is included. It is:

$$d_{eq} = \sqrt{4\overline{A}} \tag{17}$$

Cumulative frequency plots of the pore area or the aspect ratio should ideally have different shapes. The goal for the pore area, shown in Fig. 14 b), is to quickly reach a cumulative relative frequency of 1, indicating that the pores tend to be small. For the aspect ratio, depicted in Fig. 14c), the target range is 1 on the x-axis, so that the curve representing more spherical pores stays close to 0 and rapidly approaches 1 as the aspect ratio nears 1. Thus, white noise proves to be a better sonication mode compared to 1000 Hz, as the courses are closer to the target range and the equivalent pore diameter decreases when compared to the standard L-PBF modes MSH and OSH. Even though 200 Hz appears to produce smaller pores, they tend to form an irregular shape, so that they promote anisotropies.

In conjunction with the process-related pore formation mechanisms from [6,40,42] the acoustic effect can be analyzed in more detail. Appropriate L-PBF parameters as in the parameter set used here, minimize porosity originating from balling or lack of fusion anyway. However, the influence of sound on these phenomena is still unclear, as sound terms may be included in the energy density definition. Further fundamental investigations must clarify this issue. Nevertheless, the measurement data show that large and irregularly shaped pores occur in smaller proportions in assisted L-PBF than in standard L-PBF.

Common techniques to decrease porosity in additively manufactured metal parts range from closed-loop control strategies [43] or process monitoring [44] during build jobs and post-processing like hot isostatic pressing (HIP) [45,46]. The in-process approaches aim to correlate melt pool temperatures with e.g. pyrometric signals [47] and assign these to part quality. Forien et al. [48] reduced, by that, the probability of keyhole pore formation to approximately 5 % helping to adjust process parameters. However, this does not eliminate pore formation in general. Combinations of in-process approaches and sonication might lead to further reduction of porosity. HIP uses high temperature and high pressure to close pores inside parts and thereby consumes large amounts of energy. Geenen et al. [46] report non-porous parts after HIP of stainless steel samples produced via L-PBF at 1150 °C for one hour and followed by densification at 150 MPa for three hours. Herzog et al. [45] managed to increase the relative density of L-PBF-TiAl6V4 by HIP to 99.8 % at 820 °C and 200 MPa for two hours. The effect of HIP becomes

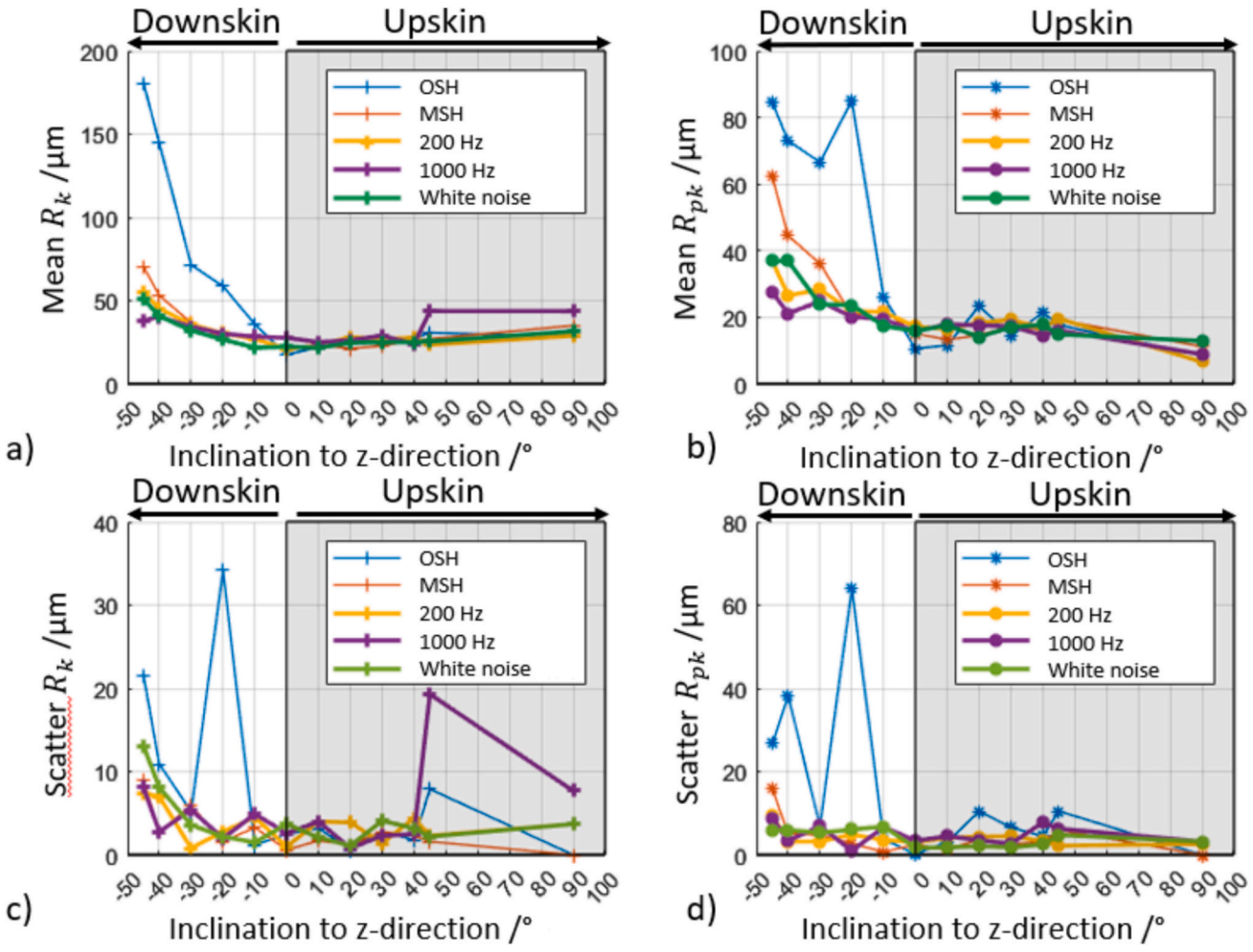

Fig. 15. Mean and scatter of surface roughness parameters R_k and R_{pk} on fan samples for different standard and assisted L-PBF modes.

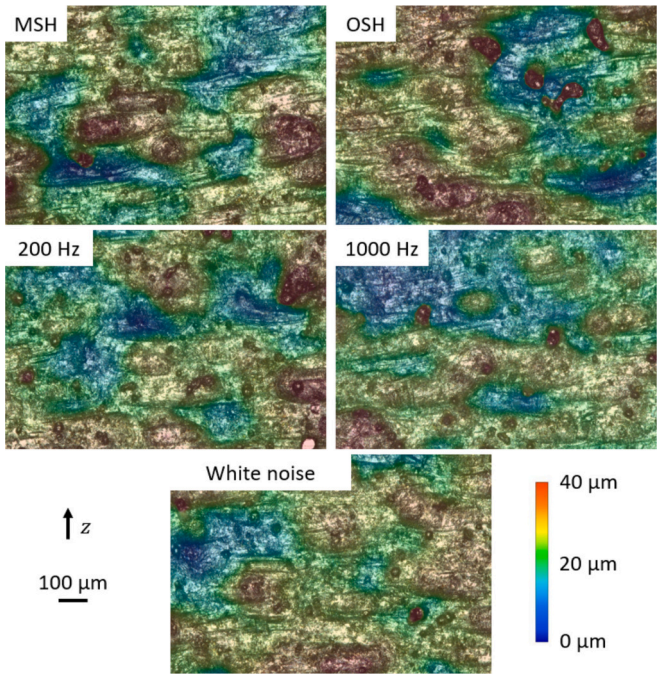

Fig. 16. Surface topography on side faces of cube samples from different standard and acoustically assisted L-PBF modes.

obvious in literature, but large amounts of energy are required to maintain these temperatures and pressures. Furthermore, HIP slows the production chain by several hours, which makes AM even slower and less attractive.

5.2. *Surface quality*

Powder-bed compaction shall decrease surface roughness. The fan samples show a progression of surface roughness over the angle of inclination of upskin and downskin surfaces. Its critical angle, at which support structures must be used, must not be exceeded in order to measure as-built surfaces. Fig. 15 illustrates that Sono-L-PBF not only compensates for the disadvantage of the lack of substrate heating but also provides better surfaces than the standard modes. The core roughness with respect to the profile center R_k, see Fig. 15 a), is similar for all sound modes and close to the MSH mode. With strong inclinations, however, sonication reduces the downskin effect. The differences are more noticeable in the peak area of the roughness profile R_{pk}, see Fig. 15 b). Curves follow less a hyperbolic path with assisted L-PBF than with standard L-PBF. The reason for this is the reduced particle adhesion to downskin surfaces, which is noticeable in a direct comparison of the samples with the naked eye. Additionally, the powder-bed probably has a greater supporting effect due to its compaction. As shown in Fig. 15 c) and d), the roughness scatter in assisted L-PBF parts is in similar regions to that in standard L-PBF parts.

Especially for upskin and downskin surfaces with a low angle of inclination, the roughness of acoustically assisted L-PBF parts hardly

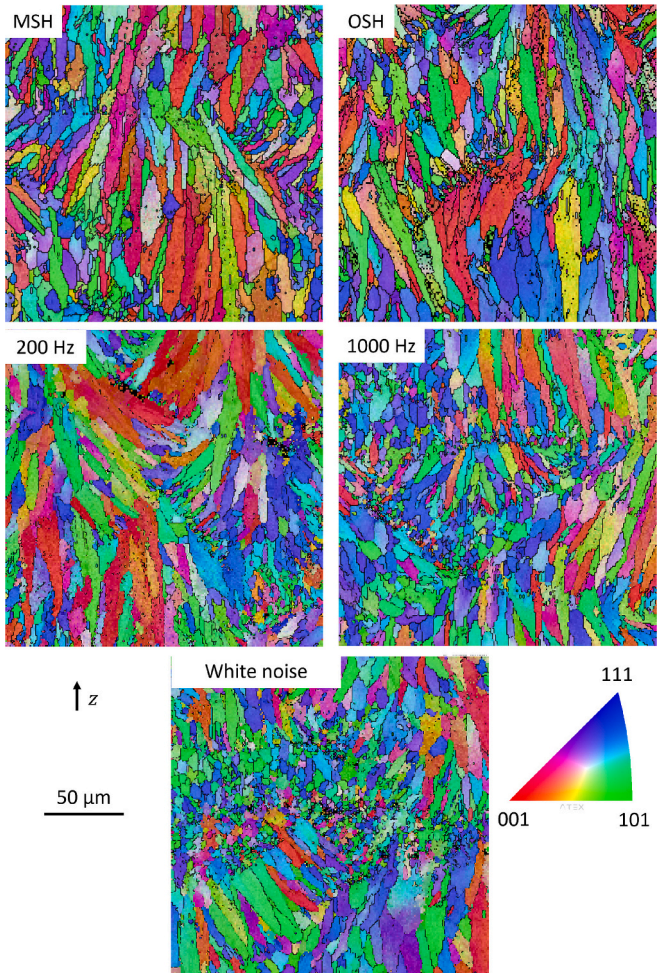

Fig. 17. EBSD grain orientation maps of different L-PBF modes.

differs from that of the standard MSH. The staircase effect is the main reason for the roughness development in these areas, which, with increasing inclination in the downskin area, is replaced by particle adhesion as the driving mechanism. Nevertheless, varying degrees of particle adhesion also occur on surfaces inclined at 0° to the z-direction, for example the side faces of the density cubes. Sonication apparently produces the most uniform surfaces and shows the less particle adhesions on the surface if compared to standard L-PBF samples.

Literature indicates that closed-loop control systems can help to reduce surface roughness. Fleming et al. [49] report on smoothed surfaces by several micrometers when image processing defines peaks of a surface profile during the L-PBF process, which are ablated, and when it defines valleys of a surface profile during the L-PBF process, which are refilled. This is a suitable method for surface smoothing, but this approach slows build jobs, if built parts of layers have to be ablated and refilled again.

Side faces of cube samples were analyzed with 3D panoramic imaging using the digital microscope, displaying differences in surface topography depending on the L-PBF mode. Images consist of a superposition of the real image and topography color codes. Even if all sonication performed almost equally upon the evolution of roughness at different inclinations, Fig. 16 proves 1000 Hz and white noise sonication to produce superior surface quality due to the least occurrences of orange or red regions.

5.3. Microstructure

The presence of acoustic vibrations during solidification shall create

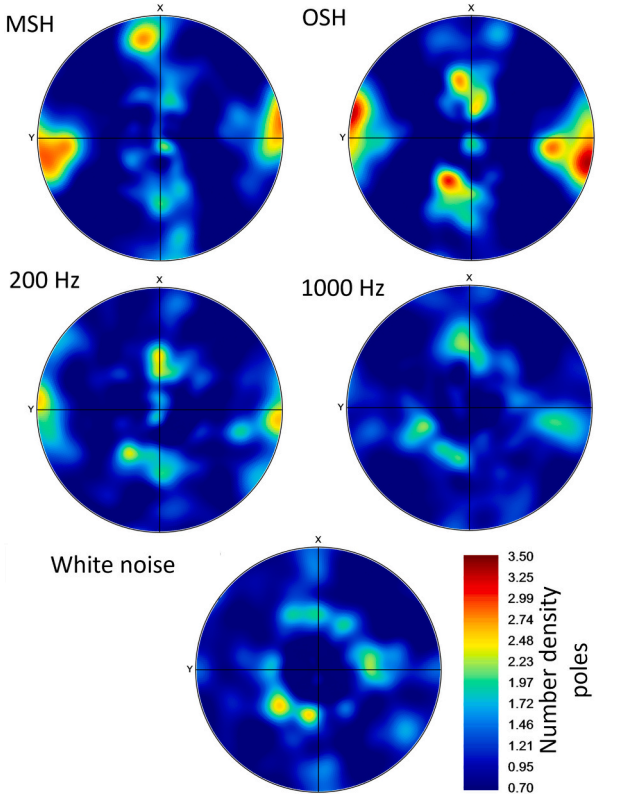

Fig. 18. (100) pole figures from EBSD data of different L-PBF modes.

an impact on microstructural formation due to its acoustic energy contributing to nucleation rate and leading to smaller and more isotropic grains. EBSD grain orientation maps in Fig. 17 represent the orientations of individual grains. Black spots result from data gaps where the measurement software was unable to create an indexing. All indexing rates exceed 90 % after noise reduction with ATEX software [31]. The effect of sonication on the microstructure is stronger in assisted LMD due to ultrasound-related cavitation and tremendous power levels. With assisted L-PBF as presented in this study, there is no cavitation and acoustic power is much lower. However, sound propagates not only through the powder-bed where attenuation occurs at every particle-particle interface but also through the part being built. Each part is fixed to the substrate to remove heat from the laser scan tracks, so sound can travel with much less attenuation through the part to the molten phase. Throughout permanent sonication, each part vibrated permanently, so solidification is influenced by vibrations at any time.

The color impression of the EBSD maps suggests that there are fewer similar orientations in the microstructure of assisted L-PBF parts if compared to standard L-PBF modes. This assumption can be verified using pole figures created by the ATEX software [31] from EBSD raw data. The calculated pole figures represent a number density of (100) poles of a stereographic projection of the occurring orientations. The formation of more pronounced regular patterns and the appearance of more intense hotspots indicate a stronger texture or anisotropy within the microstructure.

Fig. 18 illustrates the differences in the as-built state between standard and assisted L-PBF. For MSH and OSH, the pole figures display a cross-shaped pattern that weakens at 200 Hz and disappears at 1000 Hz. White noise appears to produce a different form of preferential orientation, since a more ring-shaped pattern appears in the pole figure. Apparently, assisted L-PBF reduces preferred orientations in the microstructure compared to standard L-PBF and thus results in structural anisotropy, which is expressed in equally anisotropic mechanical

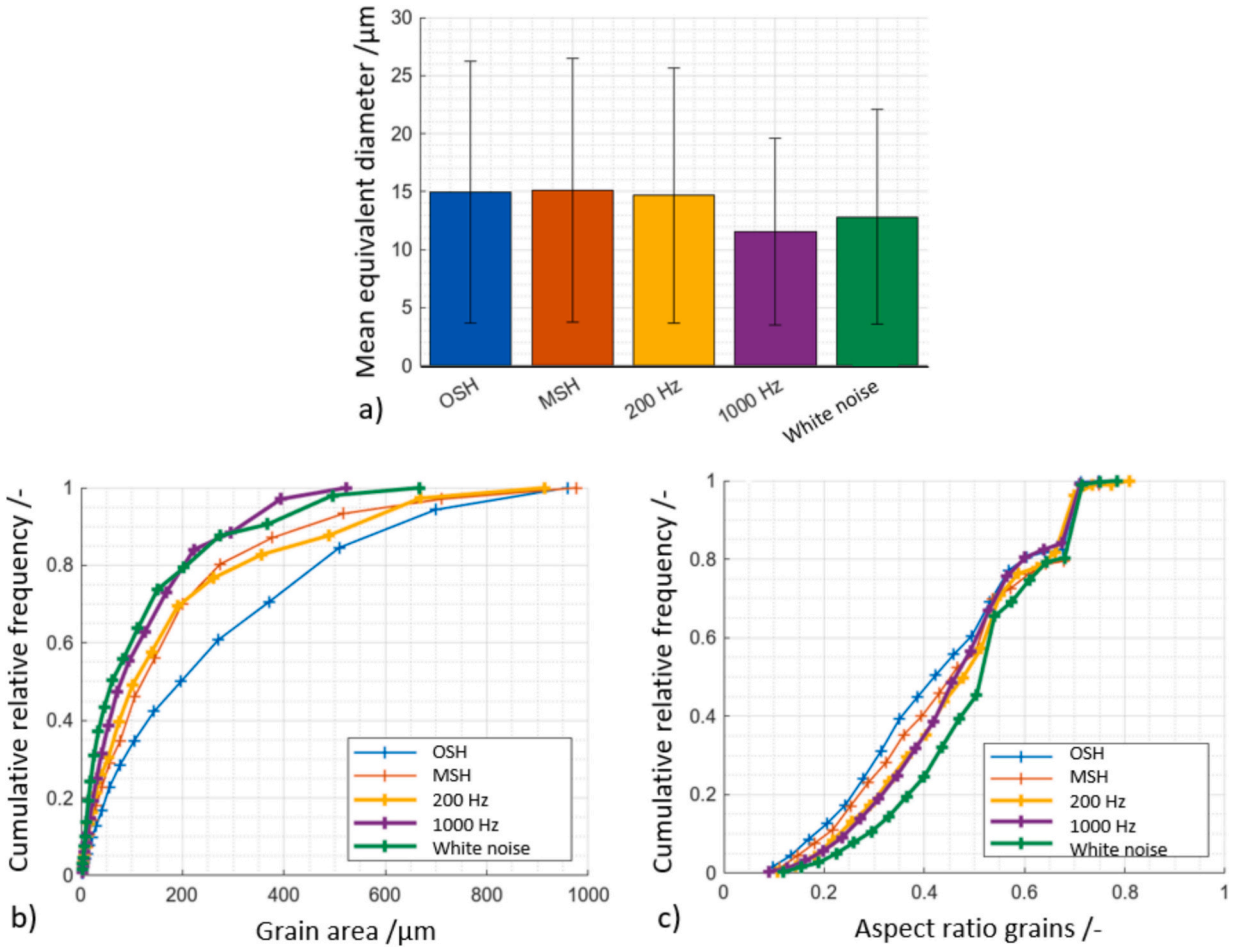

Fig. 19. Statistical grain analysis of grain ID maps from EBSD grain orientation maps a) mean equivalent diameter, b) grain area distribution and c) aspect ratio distribution.

behavior of parts. It remains to be clarified whether the nevertheless occurring columnar crystal growth can be suppressed or pushed to a further limit due to higher acoustic power, which the current system cannot achieve.

Morphology and grain size of the microstructure quantify the extent to which acoustic assistance suppresses columnar crystal growth or supports crystallization through a higher nucleation rate. For this purpose, the EDAX OIM Analysis software converts each orientation map into a grain ID map by filling data gaps and coloring neighboring grains in strong color contrast. In contrast to grain orientation maps, colors in grain ID maps do not contain any information other than distinguishability. The software then automatically calculates frequency distributions of grain areas and aspect ratios. Analogous to the evaluation of porosity, equivalent diameters are used to compare the average grain size.

Data presented by Fig. 19 reveal significant differences in the microstructure. Equivalent grain diameters of the standard L-PBF modes, as seen Fig. 19 a), do not differ from each other or from L-PBF assisted with 200 Hz. Once again, a close competition crystallizes between two assisted L-PBF modes at 1000 Hz and with white noise, whereby 1000 Hz has a narrower scattering range and has a smaller equivalent grain diameter. Cumulative relative frequency plots of grain areas, as seen in Fig. 19 b), also confirm the grain refinement by assisted L-PBF with 1000 Hz and white noise, because both curves increase more strongly that the others. All grains in the image section are described with smaller grain areas than with the other samples.

The description of equivalent grain diameters and grain areas overlaps morphologies in the microstructure and results in large standard deviations in equivalent diameters. The EBSD orientation maps in Fig. 17 have already given the impression that columnar crystal growth also occurs upon acoustic assistance. The aspect ratio is calculated as the minimum grain diameter (here: width) divided by the maximum grain diameter (here: length), so the aim is 1 representing perfectly gloublitic grains. Obviously, the cumulative relative frequency plots of aspect ratios, as seen in Fig. 19 c), increase later and more steeply for assisted L-PBF than for standard L-PBF. This observation applies in particular to white noise. As assumed, sonication tends to cause a more globulitic microstructure due to higher nucleation rates, but it cannot suppress columnar crystal growth due to steep temperature gradients from the laser incidence to the substrate. If it is possible to combine sonication with substrate heating in future studies, the temperature gradient flattens out and, together with sonication, can probably further increase the aspect ratios in the microstructure.

6. Conclusions and future studies

This contribution describes an acoustically assisted additive manufacturing process implemented in am L-PBF setup. The findings align with results presented in the literature for sonicated LMD. The main conclusions are:

- Metallic powder materials can compact by the amount of their Hausner ratio in presence of acoustic vibrations. The degree to which a powder-bed absorbs acoustic energy depends on the acoustic acceleration and the frequency. Even if there are several regions of strong energy dissipation, qualitative flowability analysis proved

that compaction is a possible but no necessary consequence of dissipation or particle damping due to spatial acceleration distributions. Both dissipation and compaction, should be clarified by experiments before choosing a proper transducer.

- Analytical derivation of a spatial powder compaction distribution of a powder-bed aligns well with experiments and reveals a possible source of property gradients inside parts of acoustically assisted L-PBF due to the sphericity of acoustic waves and their decay behavior depending on the distance from the transducer. However, the experiments with assisted L-PBF parts did not reveal such gradients.
- Adjustments to machine components enabled the implementation of an acoustic assistance setup as an expansion kit for a state-of-the-art L-PBF machine (SLM125, Nikon SLM Solutions AG) with a build volume of 60 mm in diameter and 35 mm in height. Internal cabling does not interfere with other machine functions like the recoater movement. Cable routes out of the build chamber work and do not harm gas tightness.
- Alternating layers of reverberant and absorbing materials reduce the acoustic power transfer from the transducer to the L-PBF machine to a minimum. The setup used in this study left the L-PBF unharmed.
- Best sonication modes for acoustically assisted L-PBF of AlSi10Mg are 1000 Hz and white noise, whereas white noise slightly outperforms 1000 Hz and provides a larger potential to transfer this technique to other alloys due to the application of multiple frequencies.
- Acoustically assisted L-PBF parts show significant improvements in porosity, achieving relative density values close to 100 %. As CT scans prove, there are still some pores, but they form smaller and much less numerous. Higher surface quality of L-PBFed parts suggests that interlayer roughness decreases, which in turn inhibits pore formation caused by inhomogeneous layer thickness on the previously built surface.
- Sonication of the liquid phase leads to refined grains and less textured microstructure especially for 1000 Hz and white noise. Columnar crystal growth continues to dominate microstructural formation. However, the presence of sound noticeably decreases anisotropy.
- Smoother surfaces, especially in downskin regions, originate from reduced roughness in the peak region of surface profiles due to much less particle adhesion on part surfaces. Roughness also decreases in the center roughness profiles.
- In summary, sound creates an impact in L-PBF by powder-bed compaction and melt sonication during solidification. It thereby enhances surface quality, density and microstructure.

Future studies should prove statistical confidence of these findings. These first promising results still require the determination of threshold displacements of sound the clear relationships between acoustic power and part quality which is likely to be non-linear. The impact on more complex shapes and therefore more complex sound propagation with respect to structural integrity can bring assisted L-PBF closer to application. Especially filigree or lattice structures are of interest for the application of acoustically assisted L-PBF. This study used a parameter set, which is known to produce parts of comparably high quality with standard L-PBF, but it is not sure that this is the optimal parameter with acoustic assistance. If this technique shall proceed to industrial application, it requires larger build volumes, and therefore larger transducers of higher power emission.

Transfer to other alloy systems requires a basic set of powder characterization including powder moisture content, flowability, apparent density and particle damping. Then, with an adaptable transducer as used in this study, assisted L-PBF can be tested with adjusted sonication.

CRediT authorship contribution statement

O. Maurer: Writing – original draft, Visualization, Software, Resources, Methodology, Investigation, Data curation, Conceptualization. **D. Bähre:** Writing – review & editing, Validation, Supervision, Project administration, Funding acquisition.

Declaration of competing interest

The authors declare that they have no known competing financial interests or personal relationships that could have appeared to influence the work reported in this paper.

Acknowledgements

The authors thank the European Regional Development Fund (ERDF) for supporting their research within the project number 14.2.1.4/2021/1.

The L-PBF machine used to produce the specimens in this contribution was generously funded by Deutsche Forschungsgemeinschaft (DFG) in the State Major Instrumentation program with the reference INST 256/503-1 FUGG.

The authors thank Bashar Ibrahim and Michael Becker at Fraunhofer IZfP, Saarbrücken, Germany, for the collaboration with particle damping experiments as well as Maike Jordt and Jonas Rauber from the Department of Materials Science and Technology for their support with EBSD measurements.

References

[1] Gibson I, Rosen D, Stucker B, Khorasani M. Additive manufacturing technologies. Cham: Springer International Publishing; 2021. https://doi.org/10.1007/978-3-030-56127-7.
[2] Frazier WE. Metal additive manufacturing: a review. J Mater Eng Perform 2014;23(6):1917–28. https://doi.org/10.1007/s11665-014-0958-z.
[3] Simoni F, Huxol A, Villmer F-J. Improving surface quality in selective laser melting based tool making. J Intell Manuf 2021;32(7):1927–38. https://doi.org/10.1007/s10845-021-01744-9.
[4] Rott S, Ladewig A, Friedberger K, Casper J, Full M, Schleifenbaum JH. Surface roughness in laser powder bed fusion – interdependency of surface orientation and laser incidence. Addit Manuf 2020;36:101437. https://doi.org/10.1016/j.addma.2020.101437.
[5] Uzan NE, Shneck R, Yeheskel O, Frage N. Fatigue of AlSi10Mg specimens fabricated by additive manufacturing selective laser melting (AM-SLM). Mater Sci Eng A 2017;704:229–37. https://doi.org/10.1016/j.msea.2017.08.027.
[6] Ferro P, Meneghello R, Razavi SMJ, Berto F, Savio G. Porosity inducing process parameters in selective laser melted AlSi10Mg Aluminium alloy. Phys Mesomech 2020;23(3):256–62. https://doi.org/10.1134/S1029959920030108.
[7] Romano S, Brückner-Foit A, Brandão A, Gumpinger J, Ghidini T, Beretta S. Fatigue properties of AlSi10Mg obtained by additive manufacturing: defect-based modelling and prediction of fatigue strength. Eng Fract Mech 2018;187:165–89. https://doi.org/10.1016/j.engfracmech.2017.11.002.
[8] Hyer H, et al. Understanding the laser powder bed fusion of AlSi10Mg alloy. Metallogr Microstruct Anal 2020;9(4):484–502. https://doi.org/10.1007/s13632-020-00659-w.
[9] Zhang, et al. Ultrasonic-assisted laser metal deposition of the Al 4047Alloy. Metals 2019;9(10):1111. https://doi.org/10.3390/met9101111.
[10] Li C, Sun S, Liu C, Lu Q, Ma P, Wang Y. Microstructure and mechanical properties of TiC/AlSi10Mg alloy fabricated by laser additive manufacturing under high-frequency micro-vibration. J Alloys Compd 2019;794:236–46. https://doi.org/10.1016/j.jallcom.2019.04.287.
[11] Ponnusamy P, Rahman Rashid RA, Masood SH, Ruan D, Palanisamy S. Mechanical properties of SLM-printed Aluminium alloys: a review. Materials 2020;13(19):4301. https://doi.org/10.3390/ma13194301.
[12] Todaro CJ, et al. Grain structure control during metal 3D printing by high-intensity ultrasound. Nat Commun 2020;11(1):142. https://doi.org/10.1038/s41467-019-13874-z.
[13] Todaro CJ, Easton MA, Qiu D, Brandt M, StJohn DH, Qian M. Grain refinement of stainless steel in ultrasound-assisted additive manufacturing. Addit Manuf 2021;37:101632. https://doi.org/10.1016/j.addma.2020.101632.
[14] Sánchez M, Rosenthal G, Pugnaloni LA. Universal response of optimal granular damping devices. J Sound Vib 2012;331(20):4389–94. https://doi.org/10.1016/j.jsv.2012.05.001.
[15] Baesso I, Karl D, Spitzer A, Gurlo A, Günster J, Zocca A. Characterization of powder flow behavior for additive manufacturing. Addit Manuf 2021;47:102250. https://doi.org/10.1016/j.addma.2021.102250.
[16] Saker A, Cares-Pacheco M-G, Marchal P, Falk V. Powders flowability assessment in granular compaction: what about the consistency of Hausner ratio? Powder Technol 2019;354:52–63. https://doi.org/10.1016/j.powtec.2019.05.032.

[17] Yan Z, et al. Microstructure and mechanical properties of GH5188 superalloy additively manufactured via ultrasonic-assisted laser powder bed fusion. J Alloys Compd 2023;939.
[18] Guo A, et al. Acoustic field-assisted powder bed fusion of tungsten carbide-reinforced 316L stainless steel composites. J Mater Res Technol 2023;26:5488–502. https://doi.org/10.1016/j.jmrt.2023.08.271.
[19] Maurer O, Bähre D. Quality enhancement of laser powder-bed fusion parts by acoustically assisted additive manufacturing by laser powder-bed fusion and its application to lattice structures. Adv Eng Mater 2025:2500318. https://doi.org/10.1002/adem.202500318.
[20] Sausto F, Tezzele C, Beretta S. Analysis of fatigue strength of L-PBF AlSi10Mg with different surface post-processes: effect of residual stresses. Metals 2022;12(6):898. https://doi.org/10.3390/met12060898.
[21] Bartlett JL, Li X. An overview of residual stresses in metal powder bed fusion. Addit Manuf 2019;27:131–49. https://doi.org/10.1016/j.addma.2019.02.020.
[22] Norm. NF EN ISO 4490:2018 - metallic powders - determination of flow rate by means of a calibrated funnel (hall flowmeter). 2018.
[23] Mittellehner M, Danninger H, Gierl-Mayer C, Gschiel H. Investigation of the influence of powder moisture on the spreadability using the spreading tester. Berg Huettenmaenn Monatsh 2021;166:14–22.
[24] Standard. EN ISO 3923-1:2018–10, metallic powders - determination of apparent density - part 1: funnel method (ISO 3923-1:2018); German version EN ISO 3923-1:2018. Beuth Verlag GmbH; 2018. https://doi.org/10.31030/2823249.
[25] Norm. NF ISO 3953:2011 - metallic powders - determination of tap density. 2011.
[26] Maurer O, Herter F, Bähre D. Tolerancing the laser powder bed fusion process based on machine capability measures with the aim of process control. J Manuf Process 2022;80:659–65. https://doi.org/10.1016/j.jmapro.2022.06.031.
[27] Maurer O, Jacob H, Bähre D. Reuse of Smoulder in laser powder-bed fusion of AlSi10Mg—powder characterization and sample analysis. Powders 2024;3(2):154–67. https://doi.org/10.3390/powders3020010.
[28] Nikon SLM Solutions. Material data sheet Al-alloy AlSi10Mg / EN AC-43000 / EN AC-AlSi10Mg. 2019.
[29] Fedorov A, et al. 3D slicer as an image computing platform for the quantitative imaging network. Magn Reson Imaging 2012;30(9):1323–41. https://doi.org/10.1016/j.mri.2012.05.001.
[30] Mahr. Mahrsurf surface texture parameters [Online]. Available, https://capps.mahr.com/mahr-parameter/html/english/MarSurf/MarSurf.html.
[31] Beausir B, Fundenberger J-J. ATEX-software. Metz: Université de Lorraine; 2017 [Online]. Available: www.atex-software.eu.
[32] Aboulkhair NT, Everitt NM, Ashcroft I, Tuck C. Reducing porosity in AlSi10Mg parts processed by selective laser melting. Addit Manuf 2014;1:77–86. https://doi.org/10.1016/j.addma.2014.08.001.
[33] Riener K, et al. Influence of particle size distribution and morphology on the properties of the powder feedstock as well as of AlSi10Mg parts produced by laser powder bed fusion (LPBF). Addit Manuf 2020;34:101286. https://doi.org/10.1016/j.addma.2020.101286.
[34] Vorlander M. Revised Relation between the Sound Power and the Average Sound Pressure Level in Rooms and Consequences for Acoustic Measurements 1995;81.
[35] Borchardt-Ott W. Crystallography: An introduction. Berlin, Heidelberg: Springer Berlin Heidelberg; 2012. https://doi.org/10.1007/978-3-642-16452-1.
[36] Steen WM. Laser material processing. London: Springer London; 1991. https://doi.org/10.1007/978-1-4471-3820-4.
[37] Şen A, Van den Bulcke J, Defoirdt N, Van Acker J, Pereira H. Thermal behaviour of cork and cork components. Thermochim Acta 2014;582:94–100. https://doi.org/10.1016/j.tca.2014.03.007.
[38] Bundesministerium des Innern und für Heimat, editor. TRLV Lärm Teil 1. Gemeinsames Ministerialblatt; 2017.
[39] The National Institute for Occupational Safety and Health (NIOSH). Noise and occupational hearing loss. Choice Rev 2015;52(08). https://doi.org/10.5860/CHOICE.188912. Online. 52-3982-52–3982.
[40] Wang T, Dai S, Liao H, Zhu H. Pores and the formation mechanisms of SLMed AlSi10Mg. Rapid Prototyp J 2020;26(9):1657–64. https://doi.org/10.1108/RPJ-02-2020-0036.
[41] Weingarten C, Buchbinder D, Pirch N, Meiners W, Wissenbach K, Poprawe R. Formation and reduction of hydrogen porosity during selective laser melting of AlSi10Mg. J Mater Process Technol 2015;221:112–20. https://doi.org/10.1016/j.jmatprotec.2015.02.013.
[42] Hastie JC, Kartal ME, Carter LN, Attallah MM, Mulvihill DM. Classifying shape of internal pores within AlSi10Mg alloy manufactured by laser powder bed fusion using 3D X-ray micro computed tomography: influence of processing parameters and heat treatment. Mater Charact 2020;163:110225. https://doi.org/10.1016/j.matchar.2020.110225.
[43] Khorasani A, Gibson I, Veetil JK, Ghasemi AH. A review of technological improvements in laser-based powder bed fusion of metal printers. Int J Adv Manuf Technol 2020;108(1–2):191–209. https://doi.org/10.1007/s00170-020-05361-3.
[44] Vasileska E, Demir AG, Colosimo BM, Previtali B. Layer-wise control of selective laser melting by means of inline melt pool area measurements. J Laser Appl 2020;32(2):022057. https://doi.org/10.2351/7.0000108.
[45] Herzog D, Bartsch K, Bossen B. Productivity optimization of laser powder bed fusion by hot isostatic pressing. Addit Manuf 2020;36:101494. https://doi.org/10.1016/j.addma.2020.101494.
[46] Geenen K, Röttger A, Theisen W. Corrosion behavior of 316L austenitic steel processed by selective laser melting, hot-isostatic pressing, and casting. Mater Corros 2017;68(7):764–75. https://doi.org/10.1002/maco.201609210.
[47] Renken V, Lübbert L, Blom H, Von Freyberg A, Fischer A. Model assisted closed-loop control strategy for selective laser melting. Procedia CIRP 2018;74:659–63. https://doi.org/10.1016/j.procir.2018.08.053.
[48] Forien J-B. Detecting keyhole pore defects and monitoring process signatures during laser powder bed fusion: a correlation between in situ pyrometry and ex situ X-ray radiography. 2020. p. 32.
[49] Fleming TG, Nestor SGL, Allen TR, Boukhaled MA, Smith NJ, Fraser JM. Tracking and controlling the morphology evolution of 3D powder-bed fusion in situ using inline coherent imaging. Addit Manuf 2020;32:100978. https://doi.org/10.1016/j.addma.2019.100978.